Predicting resilience through the lens of competing adjustments to vegetation function

Manon E.B. Sabot[1,2], Martin G. De Kauwe[3,1,2], Andy J. Pitman[1,2], David S. Ellsworth[4], Belinda E. Medlyn[4], Silvia Caldararu[5], Sönke Zaehle[5,6], Kristine Y. Crous[4], Teresa E. Gimeno[7,8], Agnieszka Wujeska-Klause[9,4], Mengyuan Mu[1,2], and Jinyan Yang[4].

[1] ARC Centre of Excellence for Climate Extremes, Sydney, NSW 2052, Australia

[2] Climate Change Research Centre, University of New South Wales, Sydney, NSW 2052, Australia

[3] School of Biological Sciences, University of Bristol, 24 Tyndall Avenue, Bristol BS81TQ, United Kingdom

[4] Hawkesbury Institute for the Environment, Western Sydney University, Penrith, NSW 2751, Australia

[5] Max Planck Institute for Biogeochemistry, Jena, Germany

[6] Michael Stifel Center Jena for Data- driven and Simulation Science, Jena, Germany

[7] Basque Centre for Climate Change (BC3), 48940 Leioa, Spain

[8] Ikerbasque, Basque Foundation for Science, 48008 Bilbao, Spain

[9] Urban Studies, School of Social Sciences, Locked Bag 1797, Penrith, NSW 2751, Australia

Contents of this file
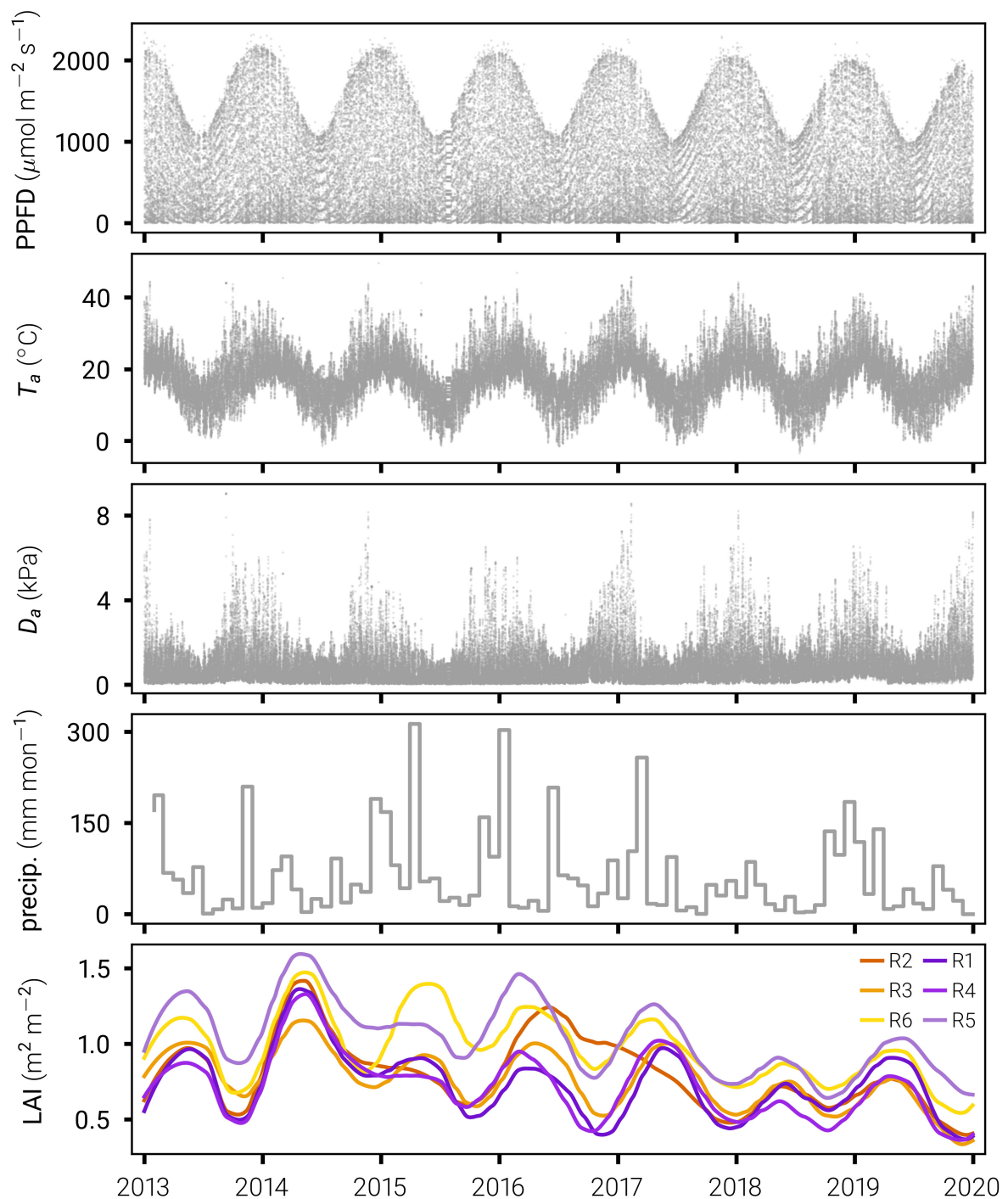
Supplementary Figures

Figure S1. Meteorological conditions and leaf area index (LAI) measured at EucFACE during the 2013 – 2020 period. From top to bottom, panels show the half-hourly photosynthetic photon flux density (PPFD), air temperature (T_a) and vapour pressure deficit (D_a), the monthly total precipitation (precip.), and the daily LAI. For the LAI, each line colour indicates a different ring, with aCO_2 rings shown in shades of orange/yellow and eCO_2 rings in shades of purple.
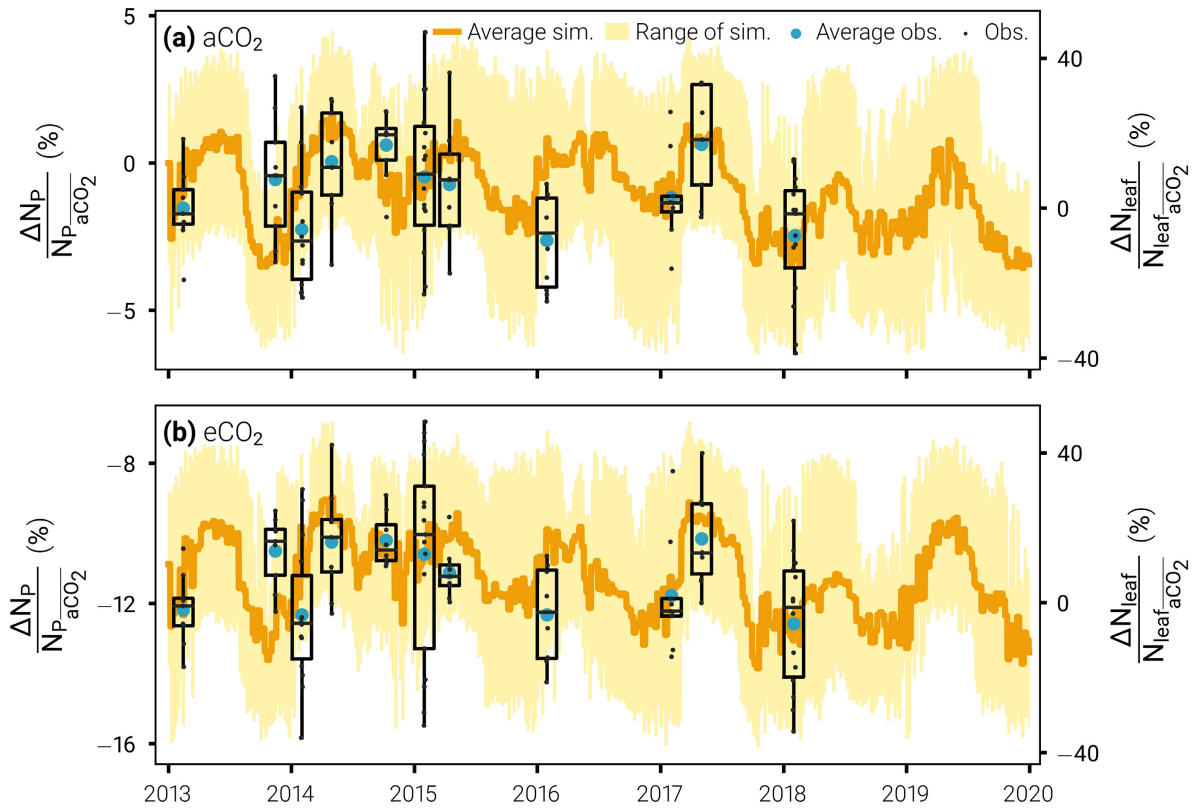
Figure S2. Timeseries of the relative change in leaf nitrogen at the aCO₂ (panel **a**) and eCO₂ (panel **b**) rings. The simulations were generated using the best model configuration (H_{leg} = 30 days, N_{opt} = 7 days) with its standard parameterisation (i.e., initialised by ring-specific $V_{cmax25_{t_0}}$ and $J_{max25_{t_0}}$). ΔN_P represents the difference between the time-varying amount of simulated leaf nitrogen directly involved in photosynthesis (N_P) and the average N_P from across the aCO₂ rings at the onset of the simulations ($N_{P_{\overline{aCO_2}}}$). Orange lines show the average relative change in N_P across rings (e.g., average of R2, R3, and R6 for the aCO₂ rings) and yellow shadings the range of simulated relative change. ΔN_{leaf} represents the difference between the time-varying amount of observed total leaf nitrogen (N_{leaf}) and the average N_{leaf} at the aCO₂ rings during the first measurement campaign in 2013 ($N_{leaf_{\overline{aCO_2}}}$). Box and whisker plots summarise the observed distributions of the relative change in N_{leaf} (line, median; box, interquartile range; whiskers, quartiles ± 1.5 times the interquartile ranges) during measurement campaigns, with each observation displayed via a dot.
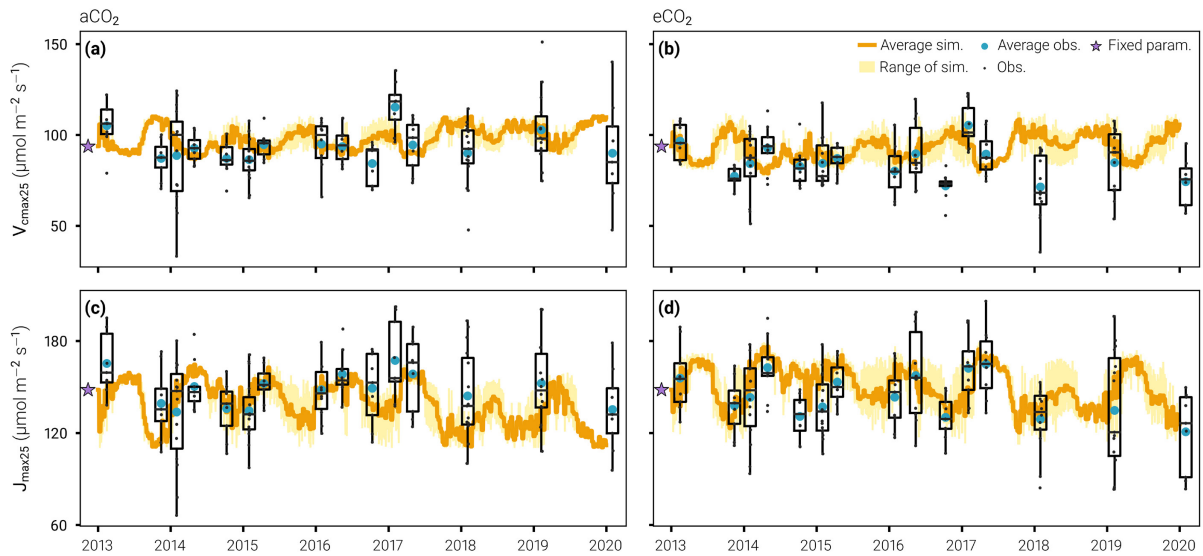
Figure S3. Timeseries of the V_{cmax25} (panels **a**, **b**) and J_{max25} (panels **c**, **d**) predicted by the best model configuration (H_{leg} = 30 days, N_{opt} = 7 days) with an alternative parameterisation (i.e., initialised by the average $V_{cmax25_{t_0}}$ and $J_{max25_{t_0}}$ from across the aCO₂ rings), and compared with field observations at the aCO₂ (panels **a**, **c**) and eCO₂ (panels **b**, **d**) rings. Orange lines show the average simulations across rings (e.g., average of R2, R3, and R6 for the aCO₂ rings) and yellow shadings the range of simulations. Box and whisker plots summarise the observed distributions of V_{cmax25} and J_{max25} (line, median; box, interquartile range; whiskers, quartiles ± 1.5 times the interquartile ranges) during measurement campaigns, with each observation displayed via a dot. Fixed parameter values appear in each panel, these refer to the aCO₂ V_{cmax25} and J_{max25} parameterisations used to test the sensitivity of the leaf nitrogen allocation scheme to its initialisation.
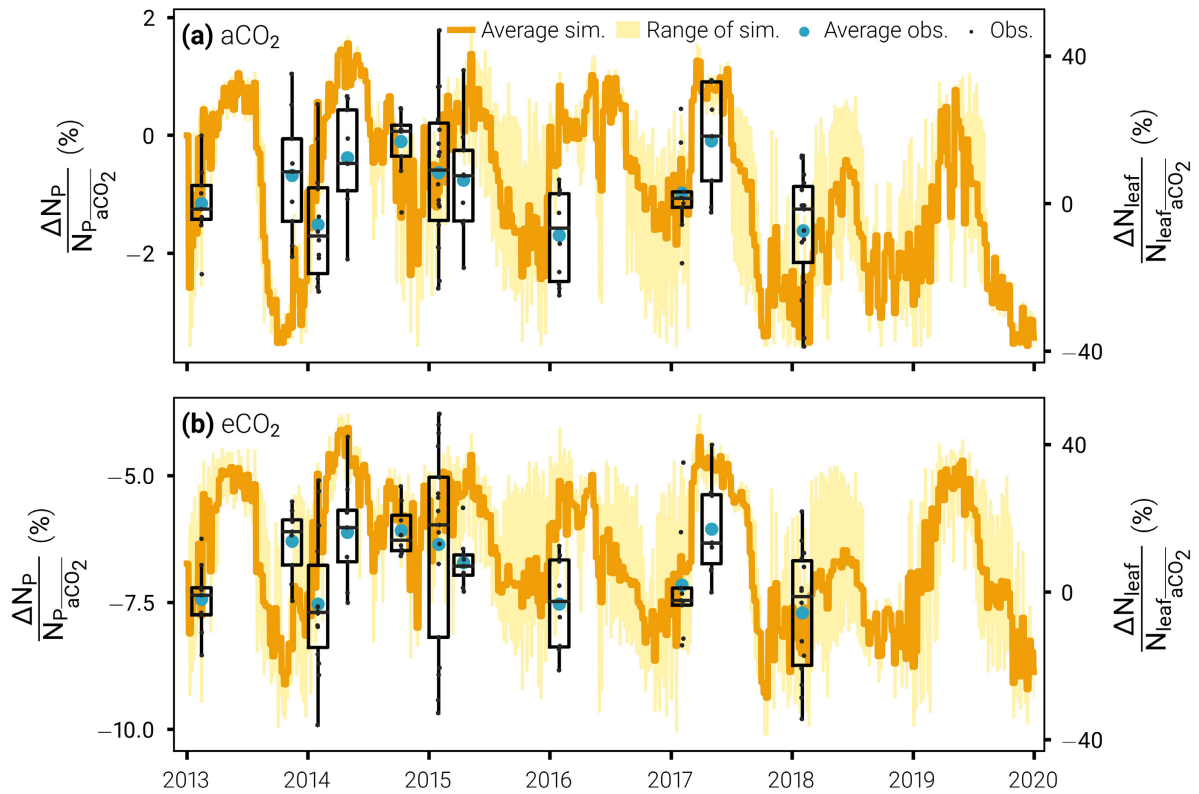
Figure S4. Timeseries of the relative change in leaf nitrogen at the aCO$_2$ (panel **a**) and eCO$_2$ (panel **b**) rings. The simulations were generated using the best model configuration (H_{leg} = 30 days, N_{opt} = 7 days) with an alternative parameterisation (i.e., initialised by the average $V_{cmax25_{t_0}}$ and $J_{max25_{t_0}}$ from across the aCO$_2$ rings). ΔN_P represents the difference between the time-varying amount of simulated leaf nitrogen directly involved in photosynthesis (N_P) and the average N_P from across the aCO$_2$ rings at the onset of the simulations ($N_{P_{\overline{aCO_2}}}$). Orange lines show the average relative change in N_P across rings (e.g., average of R2, R3, and R6 for the aCO$_2$ rings) and yellow shadings the range of simulated relative change. ΔN_{leaf} represents the difference between the time-varying amount of observed total leaf nitrogen (N_{leaf}) and the average N_{leaf} at the aCO$_2$ rings during the first measurement campaign in 2013 ($N_{leaf_{\overline{aCO_2}}}$). Box and whisker plots summarise the observed distributions of the relative change in N_{leaf} (line, median; box, interquartile range; whiskers, quartiles ± 1.5 times the interquartile ranges) during measurement campaigns, with each observation displayed via a dot.
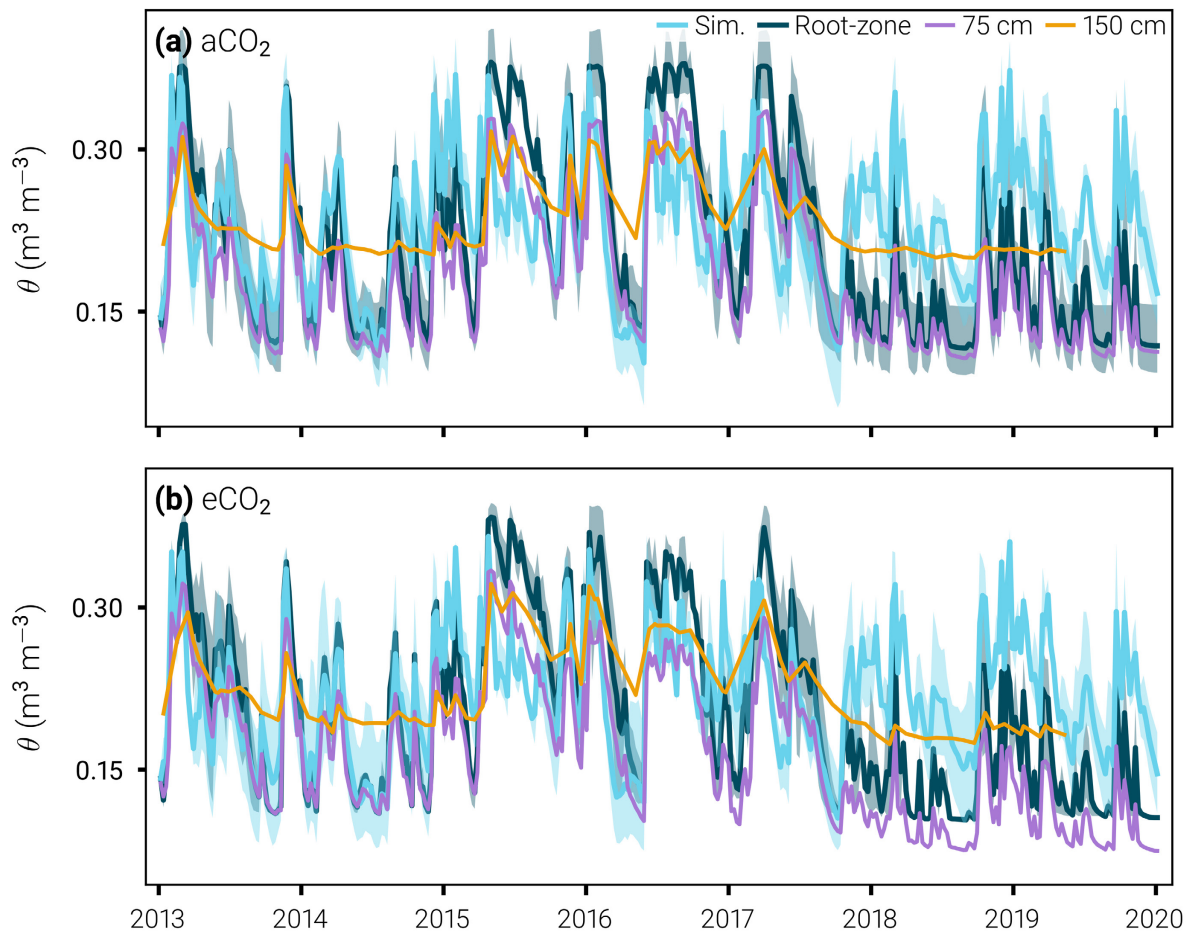
Figure S5. Weekly volumetric soil moisture (θ) simulated by the best model configuration (H_{leg} = 30 days, N_{opt} = 7 days) in the root-zone of the aCO_2 (panel **a**) and eCO_2 (panel **b**) rings. Three different observational estimates are included for comparison: (i) observations weighted by the assumed root distribution at depth (dark blue); (ii) observations averaged down to 75 cm (theta probes from 5 to 75 cm depth; purple); (iii) observations averaged down to 150 cm (neutron probes from 25 to 150 cm depth; orange). Shaded areas show the range of θ across rings for the root-zone simulated/observational estimates. Note, the default model configuration (not shown) yields simulations that strongly resemble those plotted here.
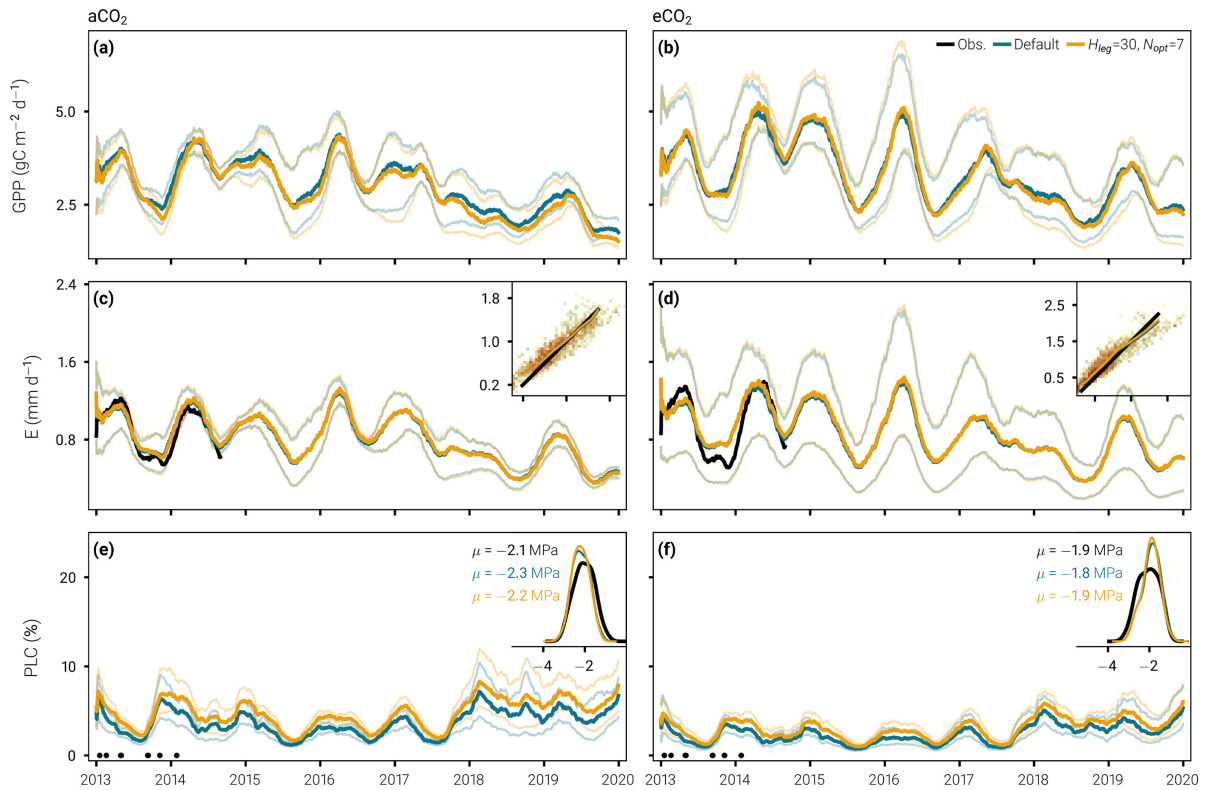
Figure S6. A comparison between the gross primary productivity (GPP; panels **a**, **b**), transpiration (E; panels **c**, **d**), and canopy percentage loss of hydraulic conductivity (PLC; panels e, **f**) simulated by the default and best (H_{leg} = 30 days, N_{opt} = 7 days) model configurations forced by estimates of root-zone soil moisture retrieved from observations at the aCO_2 (panels **a**, c, e) and eCO_2 (panels **b**, **d**, **f**) rings. In each panel, the plain lines show the average simulations across rings (e.g., average of R2, R3, and R6 for the aCO_2 rings) and the faint lines show the range of simulations. Upscaled observations of tree-level transpiration are included for comparison with the model simulations, and the insets in (c) and (**d**) show the correspondence between the daily observations (x-axis) and their paired simulated estimates (y-axis). In each of these insets, the black line corresponds to the 1:1 of the observations and coloured lines correspond to Q-Q plots of the observed to simulated transpiration. In the absence of direct observations, the simulated PLC is assessed by proxy, by comparing distributions of observed and simulated Ψ_l (morning and midday data) from the collection campaign dates marked by black dots in (e) and (**f**). These distributions, fitted via kernel density estimation, and their associated modes (μ) appear in the insets of (e) and (**f**). In all main panels (i.e., excluding the insets), the data have been smoothed with a 90-day moving window to aid visualisation.
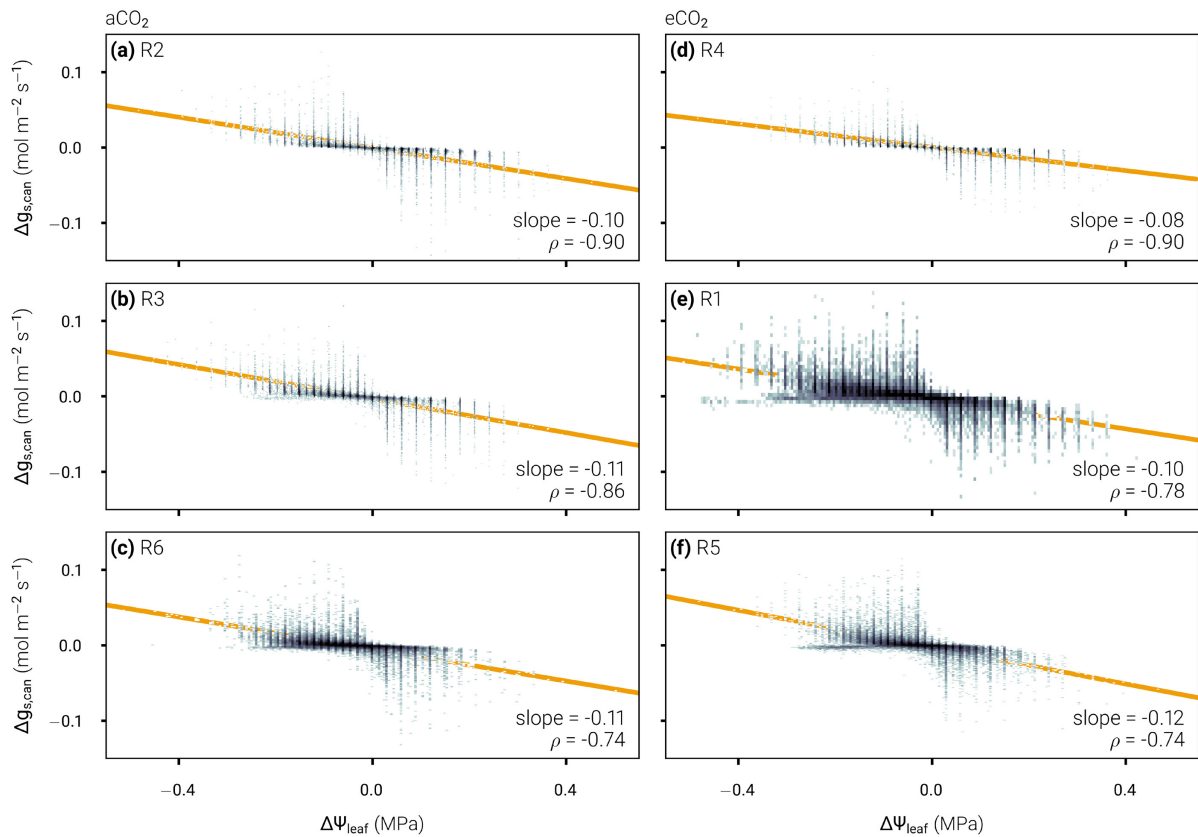
Figure S7. Sensitivity of the canopy-level stomatal conductance ($g_{s,can}$, i.e., averaging sunlit and shaded components of the canopy) to variations in leaf water potential (Ψ_{leaf}) caused by differences between the best (H_{leg} = 30 days, N_{opt} = 7 days) and the default model configurations at the aCO₂ (panels **a**, **b**, **c**) and eCO₂ (panels **b**, **e**, **f**) rings. The scatters are two-dimensional histograms of all the half-hourly $\Delta\Psi_{leaf}$ to $\Delta g_{s,can}$ pairings grouped 100 by 100, into c. 500 bins at each ring. Note, the strengths (Spearman ρ) of the $\Delta g_{s,can}\left(\Delta\Psi_{leaf}\right)$ relationships follow the ring orders from Figure 2, i.e., rank correlation becomes weaker as the average soil moisture × leaf area index increases within each panel.
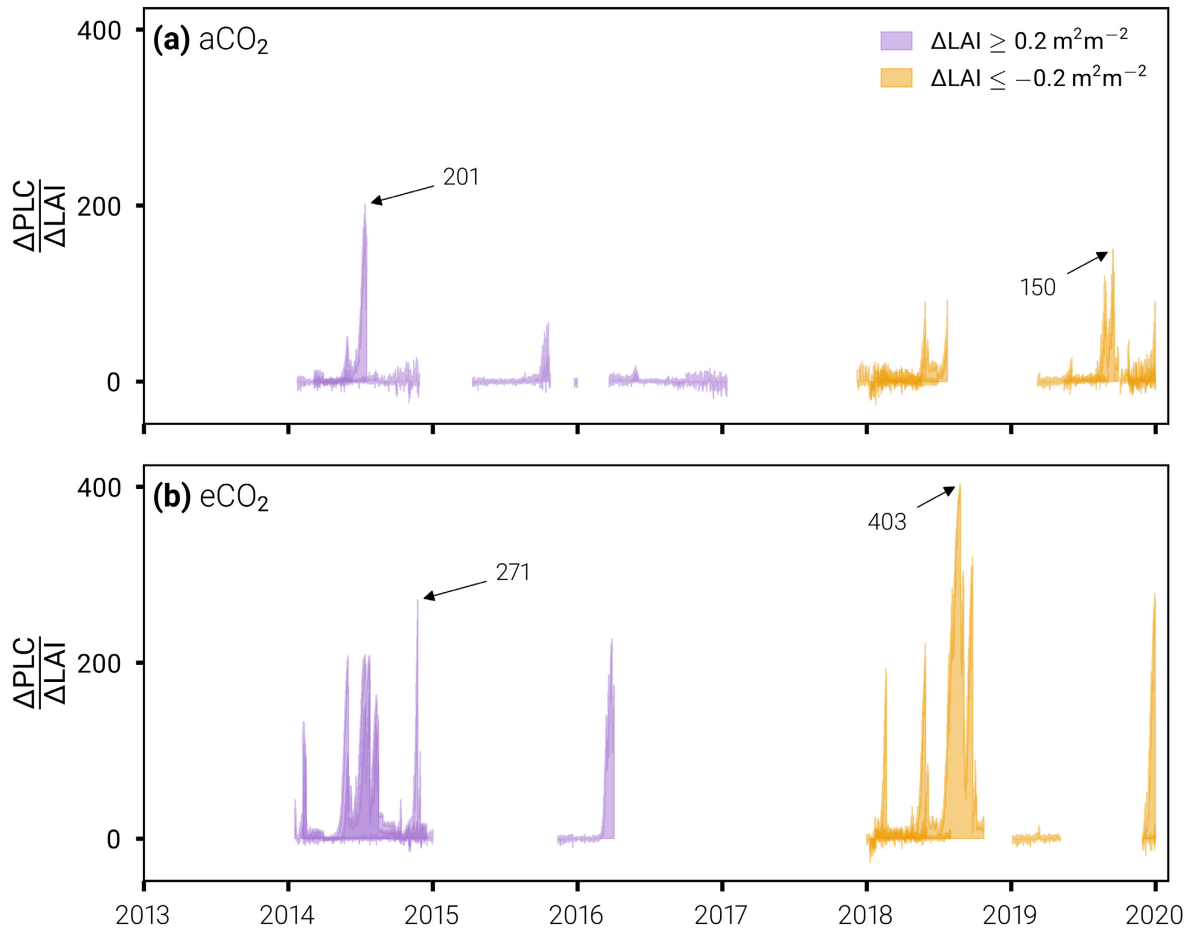
Figure S8. Ratios of percentage point differences in canopy percentage loss of hydraulic conductivity (ΔPLC; %) relative to differences in leaf area index from the average phenology (ΔLAI; m^2 m^{-2}) at the aCO$_2$ (panel **a**) and eCO$_2$ (panel **b**) rings, as simulated by the best model configuration (H_{leg} = 30 days, N_{opt} = 7 days). The data are filtered to only show the ratios associated with significant divergences in LAI, of minimum ±1/4th of the long-term LAI across rings. The maximum ratios of ΔPLC: ΔLAI are annotated on the figures for each ΔLAI category (i.e., positive ΔLAI in shades of purple vs. negative ΔLAI in shades of orange).

Supplementary Tables

Table S1. Default radiative parameters of the soil and canopy

Param.	Definitions	Units	Values
α_{ws}	Wet soil albedo	–	0.10
α_{ds}	Dry soil albedo	–	0.25
ε_s	Soil emissivity	–	0.945
$w_{l,max}$	Maximum leaf width	m	0.05
τ_l	Short wave (visible) leaf transmittivity	–	0.05
ε_l	Leaf emissivity	–	0.97
χ_l	Leaf angle distribution	$\times 10^3$	9.99999978
κ_N	Extinction coefficient of nitrogen through the canopy	–	0.001

Table S2. Default parameters of the biochemical photosynthesis model

Param.	Definitions	Units	Values
O_a	Atmospheric O_2 concentration	kPa	20.73
Γ_{25}^*	CO_2 compensation point at 25°C	Pa	4.22
K_c	Michaelis-Menten constant for carboxylation	Pa	39.96
K_o	Michaelis-Menten constant for oxygenation	kPa	27.48
E_c	Energy of activation of the carboxylation	J mol^{-1}	79430
E_o	Energy of activation of the oxygenation	J mol^{-1}	36380
E_{Γ^*}	Energy of activation of the CO_2 compensation point	J mol^{-1}	37830
H_{δ_v}	V_{cmax} rate of decrease above the optimum temperature	J mol^{-1}	200000
H_{δ_j}	J_{max} rate of decrease above the optimum temperature	J mol^{-1}	200000
α	Quantum yield of electron transport	mol photon mol^{-1} electron	0.30
h	Transition curvature factor	–	0.99

Table S3. Carbon budget parameters specific to EucFACE used in this study. The parameters were derived by Jiang et al. (2020b) from data collected at the site, they are all unitless.

		aCO$_2$	eCO$_2$
Carbon use efficiency*		0.29	0.35
Allocation coefficient	Leaves	0.48	0.45
	Wood	0.20	0.21
	Root	0.22	0.19
	Mycorrhizae	0.10	0.15

* fraction of autotrophic respiration used to convert from gross primary productivity to net primary productivity

Supplementary Methods

Methods S1. Canopy interception

In Sabot *et al.* (2020), the unitless canopy interception coefficient (r_{ci}) within the interception scheme that computes canopy evaporation and reduces the rainfall percolating through to the soil (i.e., throughfall) was a fixed percentage of incoming precipitation. We update the formulation of r_{ci} following Wang *et al.* (2008), to make it vary with the leaf area index (LAI; m² m⁻²):

$$r_{ci} = \begin{cases} 0, & R_f \leq R_{cansat} \\ 1 - e^{-(\kappa_{ci}(0.8+LAI))}, & R_f > R_{cansat} \end{cases} \quad (1.1)$$

where R_f is rainfall (mm d⁻¹), R_{cansat} (mm d⁻¹) is a minimum rainfall threshold that proxies canopy saturation, κ_{ci} (dimensionless) in as an extinction coefficient, and 0.8 (m² m⁻²) is the site branch and stem area index.

Throughfall is then simply:

$$T_f = (1 - r_{ci})\, R_f \quad (1.2)$$

And the evaporation from the top at the canopy is computed using the Penman-Monteith equation:

$$E_{ci} = r_{ci} \frac{sR_{net} + C_p g_H D_a}{(s+\gamma)\lambda} \quad (1.3)$$

where s (kPa °C⁻¹) is the slope of the saturation vapour pressure deficit of water, R_{net} (W m⁻²) is net radiation at the canopy surface, C_p (J mol⁻¹ °C⁻¹) is the specific heat capacity of dry air at constant pressure, g_H (mol m⁻² s⁻¹) is canopy conductance to heat, D_a (kPa) is atmospheric vapour pressure deficit, γ (kPa °C⁻¹) is the psychometric constant, and λ ((J mol⁻¹) is the latent heat of vaporisation.

Methods S2. Root water access

In Sabot *et al.* (2020), the water used for transpiration was extracted in a top-down order, starting from the surface layer of a six-layer water balance 'tipping bucket' scheme – the only layer to allow soil evaporation – and progressing through to the immediately next deeper layer upon depletion of each layer. In the current study, bare soil evaporation is still only supplied by the topmost soil layer, but the water used for transpiration is taken from all

layers, proportionally to root water access in each layer. Upon the dry-down of a given soil layer, its fractional root water access shifts to the nearest wettest layer. Cumulative root water access from the soil surface to depth (f_{root}; dimensionless) follows Gale & Grigal (1987):

$$f_{root} = 1 - \kappa_r{}^z \qquad (2.1)$$

where z (cm) is depth and κ_r ($1^{cm^{-1}}$) is an extinction coefficient for the root distribution.

Methods S3. Photosynthetic processes

Biochemical photosynthesis model

The net rate of carbon assimilation, A_n (µmol m^{-2} s^{-1}), is obtained from the Farquhar *et al.* (1980) biochemical photosynthesis model, including the Rubisco limited photosynthetic rate (A_c; µmol m^{-2} s^{-1}) and the RuBP regeneration limited rate (A_j; µmol m^{-2} s^{-1}), with a smoothed hyperbolic transition between these two limitations (Kirschbaum & Farquhar, 1984).

$$A_n = \frac{A_c + A_j - \sqrt{(A_c + A_j)^2 - 4\,h\,A_c\,A_j}}{2\,h} - R_d \qquad (3.1)$$

where h is a unitless transition curvature factor and R_d (µmol m^{-2} s^{-1}) is the day respiration (see Equation 3.6).

The expressions of the Rubisco limited rate, A_c (µmol m^{-2} s^{-1}), and of the electron transport limited rate were obtained from De Pury & Farquhar (1997):

$$A_c = \frac{V_{cmax}(C_i - \Gamma^*)}{C_i + K_m} \qquad (3.2)$$

where V_{cmax} (µmol m^{-2} s^{-1}) is the maximum carboxylation capacity scaled up per unit canopy area (i.e., shaded or sunlit; Wang & Leuning 1998), C_i (Pa) is the intercellular CO_2 partial pressure, Γ^* (Pa) is the CO_2 compensation point of photosynthesis. K_m (Pa) is the effective Michaelis-Menten constant:

$$K_m = K_c \left(1 + \frac{O_a}{K_o}\right) \qquad (3.3)$$

where K_c (Pa) is the Michaelis-Menten constant of Rubisco for CO_2, K_o (Pa) the Michaelis-Menten constant of Rubisco for O_2, and O_a (Pa) is the atmospheric oxygen partial pressure.

The second limitation, A_j (µmol m^{-2} s^{-1}), is expressed as:

$$A_j = \frac{J\,(C_i - \Gamma^*)}{4\,(C_i + 2\Gamma^*)} \qquad (3.4)$$

where J (µmol m^{-2} s^{-1}) is the irradiance dependence of electron transport, such that:

$$J = \frac{\alpha PPFD + J_{max} - \sqrt{(\alpha PPFD + J_{max})^2 - 4c\alpha J_{max} PPFD}}{2c} \qquad (3.5)$$

where α (mol photon mol^{-1} electron) is the effective quantum yield of electron transport depending on leaf emissivity, $PPFD$ (µmol m^{-2} s^{-1}) is the photosynthetic photon flux density, J_{max} (µmol m^{-2} s^{-1}) is the maximum rate of electron transport scaled up per unit canopy area, and c defines the unitless curvature of the leaf response of electron transport to irradiance.

The temperature dependency of Γ^*, K_c, and K_o is modelled using an Arrhenius function relative to 25 °C, as in De Pury & Farquhar (1997).

The temperature dependency of V_{cmax} and J_{max} is modelled using a peaked Arrhenius function relative to 25 °C, to account for limitations at high temperature, as in Medlyn et al. (2002). To account for low temperatures effects (i.e. below 10°C), we simply apply a linear ramp.

Finally, the day respiration is expressed following Tjoelker *et al.* (2001) at the leaf level:

$$R_d = R_{d,25}(3.22 - 0.046 - T_{leaf})^{\left(\frac{T_{leaf} - 25}{10}\right)} \qquad (3.6)$$

where $R_{d,25}$ (µmol m^{-2} s^{-1}) is the reference day respiration rate at 25°C and T_{leaf} (°C) is the leaf temperature for either the sunlit or the shaded fraction of the canopy. R_d is subsequently scaled up per unit canopy area following Wang & Leuning (1998).

Diffusive supply of CO$_2$ through the stomates

C_i is obtained by substitution of A_n from the biochemical photosynthetic model (Equation 3.1) and Fick's law of diffusion applied to the supply of CO$_2$:

$$A_n = 10^3 \frac{g_s g_b (C_a - C_i)}{1.57\left(\frac{1.35}{1.57}g_s + g_b\right)P_{atm}} \qquad (3.7)$$

where g_s (mol m^{-2} s^{-1}) is the stomatal conductance scaled per canopy element, g_b (mol m^{-2} s^{-1}) is the boundary layer conductance to water vapour, and C_a (Pa) is atmospheric [CO$_2$], P_{atm} (kPa) is atmospheric pressure. The 10^3 conversion factor accounts for the magnitude difference between the units of C_a/C_i and P_{atm} to express A_n in μmol m^{-2} s^{-1}. 1.57 converts from conductance to CO$_2$ to conductance to water vapour, whilst 1.35 converts from boundary layer conductance to CO$_2$ to boundary layer conductance to water vapour.

Methods S4. Water supply to the leaves and transpiration

Canopy transpiration

T_{leaf} and the leaf-to-air vapour pressure deficit (D_{leaf}) are expressed for each canopy element, by rearranging the Penman-Monteith energy balance function for leaves, following equation 14.6 of Campbell & Norman (1998). Canopy transpiration (E; mmol m^{-2} s^{-1}) is subsequently assumed to meet the atmospheric demand for water vapour on an instantaneous basis:

$$E = 10^3 \frac{g_s g_b D_{leaf}}{(g_s + g_b) P_{atm}} \qquad (4.1)$$

where D_{leaf} is expressed in kPa, and 10^3 converts to mmol.

Supply of water from the roots to the leaves

Ψ_l (MPa) is obtained by solving a system comprising Equation 4.1 and the steady-state supply of water from the roots to the leaves (Sperry & Love, 2015):

$$E = \int_{\Psi_s}^{\Psi_l} k_\Psi \, d\Psi \qquad (4.2)$$

where Ψ is the varying water potential between the root-zone soil water potential Ψ_s (MPa) and Ψ_{leaf}, and k_Ψ (mmol m^{-2} s^{-1} MPa^{-1}) is the associated hydraulic conductance given in Eqn. 5 of the main text. Ψ cannot drop below Ψ_{crit}, the critical threshold indicative of xylem failure at k_{crit}.

Our approach combines all hydraulic segments into a single conductor that directly connects the root-zone to the leaves, which considerably reduces parameterisation but prevents the separate solving of, for instance, xylem and leaf water potentials.

The undamaged vulnerability curve to cavitation that is either used directly in Eqn. 5 or first modified in Eqn. 6 before being used in Eqn. 5 is given by a cumulative Weibull distribution (Neufeld *et al.*, 1992):

$$f_{vc}(\Psi) = e^{-\left(\frac{|\Psi|}{s_1}\right)^{s_2}} \qquad (4.3)$$

where s_1 (MPa) and s_2 (unitless) are the sensitivity and shape of the vulnerability curve derived from reference water potential drops associated with percentages of lost xylem hydraulic conductivity:

$$s_2 = \frac{Log\left(\frac{Log(1-x_1/100)}{Log(1-x_2/100)}\right)}{Log\,P_{x_1} - Log\,P_{x_2}} \qquad (4.4)$$

$$s_1 = \frac{P_{x_1}}{(-Log(1-x_1/100))^{\frac{1}{s_2}}} \qquad (4.5)$$

where x_1 and x_2 are two percentage values of hydraulic conductivity loss and P_{x_1} and P_{x_2} their associated water potentials.

Methods S5. Leaf nitrogen stoichiometry

Following Medlyn (1996), N_p is divided into thylakoid nitrogen invested in chlorophyll-protein complexes (N_c; mol m^{-2}) and electron-transport components (N_e; mol m^{-2}), as well as soluble protein nitrogen invested in Rubisco (N_r; mol m^{-2}) and other soluble protein (N_s; mol m^{-2}).

$$N_c = \frac{0.076 a_{abs}}{25(1-a_{abs})} \qquad (5.1)$$

where a_{abs} (unitless; see notes below Table 1) is the absorptance of photosynthetic photon flux density and $0.076/25$ is an empirical coefficient that characterizes the moles of nitrogen necessary to complex one mole of chlorophyll (Evans, 1989, 1993).

$$N_e = \frac{J_{max25} - b_j N_c}{a_j} \qquad (5.2)$$

where a_j (µmol mol N^{-1} s^{-1}) and b_j (µmol mol N^{-1} s^{-1}) are empirical coefficients that link electron transport rate to leaf nitrogen distribution that are taken to be 15870 and 2775, respectively (Medlyn, 1996).

$$N_r = M_{Rubisco} c_R \frac{V_{cmax25}}{\eta_{cat}} \qquad (5.3)$$

where $M_{Rubisco}$ (g µmol^{-1}) is the molar mass of Rubisco (~0.55 g µmol^{-1}), c_R is the nitrogen concentration in Rubisco (~1.14 × 10^{-2} mol N g Rubisco^{-1}) and η_{cat} is the specific activity of Rubisco (mol C mol Rubisco^{-1} s^{-1}; Table 1).

$$N_s = d_s J_{max25} \qquad (5.4)$$

where d_s (mol N m^2 s umol-1) is an empirical coefficient taken to be 1.25 × 10^{-4} (Medlyn, 1996).

At the onset of a simulation, the pools are initialised from $V_{cmax25_{t_0}}$ and $J_{max25_{t_0}}$ and with $N_p = N_c + N_e + N_r + N_s$.

Upon each call of the leaf nitrogen allocation routine (initialisation excluded), R_{d25} is reset to 1.5% of the V_{cmax25} (Collatz *et al.*, 1991) once N_p has been redistributed.

Methods S6. Model parameterisation

Parameter values of V_{cmax25}, J_{max25}, and R_{d25} were first averaged by measurement campaign and then across measurement campaigns (i.e., each campaign weighted equally), from estimates obtained from repeated light- and temperature-controlled photosynthesis-CO$_2$ response (A-C_i) curves measured between February 2013 and February 2020 (Ellsworth *et al.* 2017; Wujeska-Klause *et al.* 2019; Yang *et al.* 2020; see 'Observational datasets').

r_k was derived from measurements of Ψ_l, predawn Ψ_l (a proxy for Ψ_s), and a parameterised hydraulic vulnerability curve (see P_x in Table 1). Observations of morning and midday Ψ_l were averaged from 360 measurements made on two leaves of the same trees in each ring, at five different occasions between October 2012 and November 2013 (Gimeno *et al.* 2016; see 'Observational datasets'). Predawn Ψ_l was also recorded during those measurement campaigns. The observed water potential data were transformed into percentage loss of hydraulic conductivity through the hydraulic vulnerability curve. We then identified three distinct states of hydraulic conductivity per tree: undamaged, most damaged, and recovered. r_k was taken as the ratio of recovered to undamaged conductivity adjusted to account for damage, i.e., $\frac{recovered - most\ damaged}{undamaged - most\ damaged}$.

The soil texture and hydraulic parameters were derived via the pedotransfer functions of Cosby *et al.* (1984), from fractions of sand, clay, and silt measured at depth in each ring. To make the soil parameters representative of the root-zone, we weighted them by root fraction (Methods S2), assuming a maximum rooting depth of 175 cm with 98% of roots within 62.5 cm of the surface, in line with observations at the site (Ochoa-Hueso *et al.*, 2020).

Model parameters that could not be readily determined were calibrated from (i) canopy interception, (ii) whole-tree transpiration (i.e., not upscaled to the ring-level), and (iii) soil evaporation data collected in each ring throughout 2013 and 2014. The observations of tree-level transpiration data are briefly described in 'Observational datasets'. As for the observations of canopy interception and soil evaporation, they are constrained by combined measurements of canopy throughfall and stemflow, and by estimates of soil evaporation together with understorey transpiration (i.e., including flushing and wilting dynamics of the understorey), respectively. All data are thoroughly described in Gimeno *et al.* (2018).

We used a stochastic population algorithm (i.e., Differential Evolution; Storn & Price 1997; Newville *et al.* 2019) and minimised the residual sum of squares between daily (canopy interception, soil evaporation) or weekly (transpiration) totals of each observed and modelled evaporative flux. In this way, we calibrated: (i) R_{cansat} and κ_{ci}; (ii) k_{max}; and (iii) r_{sl}. Soil moisture retrievals (see 'Observational datasets') were included as constraints on the transpiration and evaporation. To limit over-accounting for dry-down effects, we restricted the calibration of the transpiration to the 50% highest observations.

Methods S7. Evaluation metrics

The ratio of modelled to observed sample standard deviation (SD_{rel}, i.e., the relative variability) is simply:

$$SD_{rel} = \frac{\sqrt{\frac{1}{n-1}\sum_{i=1}^{n}(sim_i - \overline{sim_i})^2}}{\sqrt{\frac{1}{n-1}\sum_{i=1}^{n}(obs_i - \overline{obs_i})^2}} \qquad (7.1)$$

Values <1 characterise simulations less variable than the observations and *vice versa*. SD_{rel} is close to 1 when a model simulates adequate dispersion.

The similarity skill score (S_{score}; Perkins *et al.* 2007) calculates the cumulative minimum overlap of two binned distributions:

$$S_{score} = \sum_{i=1}^{N} \min\left(Z_{sim_i}, Z_{obs_i}\right) \qquad (7.2)$$

where N is the number of bins considered, and Z_{sim} and Z_{obs} are the modelled and observed frequencies of values in a given bin.

A S_{score} of 1 signifies a perfect simulation – i.e., a simulation that reproduces the observed conditions perfectly – whereas values close to 0 indicate little similarity between a simulation and the observations.

The Mean Absolute Scaled Error (MASE; Hyndman & Koehler, 2006) which quantifies the accuracy of a simulation is:

$$MASE = \frac{\overline{|sim-obs|}}{\frac{1}{n-1}\sum_{i=2}^{n}|obs_i-obs_{i-1}|} \qquad (7.3)$$

A MASE of 0 denotes the minimum possible simulation error and values <1 identify models more skilled than a one-step forecast of the previous observation.

Supplementary references

Collatz GJ, Ball JT, Grivet C, Berry JA. 1991. Physiological and environmental regulation of stomatal conductance, photosynthesis and transpiration: a model that includes a laminar boundary layer. *Agricultural and Forest Meteorology* 54: 107–136.

Cosby BJ, Hornberger GM, Clapp RB, Ginn TR. 1984. A Statistical Exploration of the Relationships of Soil Moisture Characteristics to the Physical Properties of Soils. *Water Resources Research* 20: 682–690.

De Pury DGG, Farquhar GD. 1997. Simple scaling of photosynthesis from leaves to canopies without the errors of big-leaf models. *Plant, Cell and Environment* 20: 537–557.

Ellsworth DS, Anderson IC, Crous KY, Cooke J, Drake JE, Gherlenda AN, Gimeno TE, Macdonald CA, Medlyn BE, Powell JR, *et al.* 2017. Elevated CO2 does not increase eucalypt forest productivity on a low-phosphorus soil. *Nature Climate Change* 7: 279–282.

Evans JR. 1989. Photosynthesis and nitrogen relationships in leaves of C3 plants. *Oecologia* 78: 9–19.

Evans J. 1993. Photosynthetic Acclimation and Nitrogen Partitioning Within a Lucerne Canopy. I. Canopy Characteristics. *Functional Plant Biology* 20: 55.

Farquhar GD, Caemmerer S von, Berry JA. 1980. A biochemical model of photosynthetic CO2 assimilation in leaves of C3 species. *Planta* 149: 78–90.

Gale MR, Grigal DF. 1987. Vertical root distributions of northern tree species in relation to successional status. *Canadian Journal of Forest Research* 17: 829–834.

Gimeno TE, Crous KY, Cooke J, O'Grady AP, Ósvaldsson A, Medlyn BE, Ellsworth DS. 2016. Conserved stomatal behaviour under elevated CO_2 and varying water availability in a mature woodland (D Whitehead, Ed.). *Functional Ecology* 30: 700–709.

Gimeno TE, McVicar TR, O'Grady AP, Tissue DT, Ellsworth DS. 2018. Elevated CO_2 did not affect the hydrological balance of a mature native *Eucalyptus* woodland. *Global Change Biology* 24: 3010–3024.

Hyndman RJ, Koehler AB. 2006. Another look at measures of forecast accuracy. *International Journal of Forecasting* 22: 679–688.

Jiang M, Medlyn BE, Drake JE, Duursma RA, Anderson IC, Barton CVM, Boer MM, Carrillo Y, Castañeda-Gómez L, Collins L, *et al.* 2020. The fate of carbon in a mature forest under carbon dioxide enrichment. *Nature* 580: 227–231.

Kirschbaum M, Farquhar G. 1984. Temperature Dependence of Whole-Leaf Photosynthesis in Eucalyptus pauciflora Sieb. Ex Spreng. *Functional Plant Biology* 11: 519.

Medlyn BE. 1996. The Optimal Allocation of Nitrogen Within the C_3 Photosynthetic System at Elevated CO_2. *Australian Journal of Plant Physiology* 23: 593.

Medlyn BE, Dreyer E, Ellsworth D, Forstreuter M, Harley PC, Kirschbaum MUF, Le Roux X, Montpied P, Strassemeyer J, Walcroft A, *et al.* 2002. Temperature response of parameters of a biochemically based model of photosynthesis. II. A review of experimental data. *Plant, Cell and Environment* 25: 1167–1179.

Neufeld HS, Grantz DA, Meinzer FC, Goldstein G, Crisosto GM, Crisosto C. 1992. Genotypic Variability in Vulnerability of Leaf Xylem to Cavitation in Water-Stressed and Well-Irrigated Sugarcane. *Plant Physiology* 100: 1020–1028.

Newville M, Otten R, Nelson A, Ingargiola A, Stensitzki T, Allan D, Fox A, Carter F, Michał, Pustakhod D, *et al.* 2019. *lmfit/lmfit-py 1.0.0*. Zenodo.

Ochoa-Hueso R, Piñeiro J, Power SA. 2020. Spatial distribution of fine root biomass in a remnant Eucalyptus tereticornis woodland in Eastern Australia. *Plant Ecology* 221: 55–62.

Perkins SE, Pitman AJ, Holbrook NJ, McAneney J. 2007. Evaluation of the AR4 Climate Models' Simulated Daily Maximum Temperature, Minimum Temperature, and Precipitation over Australia Using Probability Density Functions. *Journal of Climate* 20: 4356–4376.

Sperry JS, Love DM. 2015. What plant hydraulics can tell us about responses to climate-change droughts. *New Phytologist* 207: 14–27.

Storn R, Price K. 1997. Differential Evolution – A Simple and Efficient Heuristic for global Optimization over Continuous Spaces. *Journal of Global Optimization* 11: 341–359.

Tjoelker MG, Oleksyn J, Reich PB. 2001. Modelling respiration of vegetation: evidence for a general temperature-dependent Q10. *Global Change Biology* 7: 223–230.

Wang J, Endreny TA, Nowak DJ. 2008. Mechanistic Simulation of Tree Effects in an Urban Water Balance Model [1]. *JAWRA Journal of the American Water Resources Association* 44: 75–85.

Wang Y-P, Leuning R. 1998. A two-leaf model for canopy conductance, photosynthesis and partitioning of available energy I: *Agricultural and Forest Meteorology* 91: 89–111.

Wujeska-Klause A, Crous KY, Ghannoum O, Ellsworth DS. 2019. Lower photorespiration in elevated CO_2 reduces leaf N concentrations in mature *Eucalyptus* trees in the field. *Global Change Biology* 25: 1282–1295.

Yang J, Medlyn BE, De Kauwe MG, Duursma RA, Jiang M, Kumarathunge D, Crous KY, Gimeno TE, Wujeska-Klause A, Ellsworth DS. 2020. Low sensitivity of gross primary production to elevated CO2 in a mature eucalypt woodland. *Biogeosciences* 17: 265–279.